Title: T cell Aryl Hydrocarbon Receptor Activity Tunes the Gut Microenvironment to Sustain Autoimmunity

Authors: Andrea R. Merchak,[1, 2, 3] Hannah J. Cahill,[1] Lucille C. Brown,[1] Ryan M. Brown,[1,2, 3] Courtney Rivet-Noor,[1,2, 3] Rebecca M. Beiter,[1,2, 3] Erica R. Slogar,[1] Deniz G. Olgun,[1] and Alban Gaultier[1, 3]*

Affiliations:

[1]Department of Neuroscience, University of Virginia, Charlottesville, VA, USA

[2]Neuroscience Graduate Program, University of Virginia, Charlottesville, VA, USA

[3]Center for Brain Immunology and Glia, University of Virginia, Charlottesville, VA, USA

*Corresponding author. Email: ag7h@virginia.edu.

Abstract:

Multiple sclerosis (MS) is an incurable T cell driven autoimmune disease of the central nervous system. The contribution of the environment and, in particular, the gut flora to MS etiology is well documented but not well understood. The aryl hydrocarbon receptor (AHR) binds numerous molecules present in the environment and is a therapeutic target for MS: however, its precise function in T lymphocytes, the orchestrators of MS, has not been described. Here, we show that CD4 specific *Ahr* knockout drives recovery in EAE by a decreasing T cell fitness. At the mechanistic level, we show that the absence of AHR changes the gut microenvironment composition to generate metabolites, such as bile salts and short chain fatty acids, that impact T cell viability and influence disease recovery. Our study demonstrates a newly emerging role for AHR in mediating the interdependence between T lymphocytes and the microbiota while identifying new potential molecular targets for the treatment of MS and other autoimmune diseases.

One Sentence Summary: The aryl hydrocarbon receptor modulates the gut microenvironment to promote autoimmunity in a mouse model of multiple sclerosis.

Main Text:

INTRODUCTION

Multiple sclerosis (MS) is a chronic inflammatory demyelinating disease that affects 2.3 million people worldwide. MS etiology and pathology are linked to both genetic and environmental factors(*1*). One of the most important environmental factors impacting disease pathology lies with the gut microbiota(*2–5*). Indeed, the connection between the microbiota and the immune system in autoimmune disorders such as MS is well established(*6*). The gut flora, composed of bacteria, fungi, and viruses, aids food digestion and maintains pathogen control; but, recent studies have also highlighted the integral role of the microbiome in modulation of the homeostatic immune state both locally and systemically(*7*). Gut dysbiosis is a hallmark of disease in both patients with MS and in experimental animal models of MS(*2*, *8–11*). The dysbiotic microbiome can change onset and increase disease severity in mice (*10*). Furthermore, germ-free mice lacking a microbiome are resistant to experimental autoimmune encephalomyelitis (EAE), an animal model of MS(*12*). These findings spurred the examination of various bacterial supplements in mouse models of MS, and numerous potential candidates have been identified(*6*, *13*). However, the mechanism(s) of action is not well understood. The importance of the microbiome in MS is well described, but a better understanding of the cross-talk between the immune system and the microbiome is required to translate these findings to the clinic.

The aryl hydrocarbon receptor (AHR) is a prime candidate for understanding the microbiome-immune interface. The AHR is a cytoplasmic receptor that, when activated, traffics

to the nucleus to execute downstream transcriptional programing(*14*). While most of the canonical immune sensors respond exclusively to pathogenic material, the AHR is a homeostatic regulator that is activated by a variety of exogenous ligands present in barrier tissues. These ligands include indoles(*15*), kynurenines(*16*), and other small molecules(*17*) and downstream immune effects are dependent on the cell type and ligand. The AHR has also been directly tied to MS. AHR activation is the suspected mechanism by which the novel MS therapeutic, Laquinimod, acts(*18*, *19*). It is thought that AHR activation by Laquinimod in antigen presenting cells reduces the ratio between inflammatory T cells and regulatory T cells (Treg). Microbiome changes have been identified in AHR null mice and in mice treated with a potent AHR agonist 2,3,7,8-tetrachlorodibenzo-p-dioxin (TCDD), further supporting the connection between AHR, the microbiome and MS (*20–24*). While AHR activity in response to microbiome derived metabolites is well described, the reverse is not well understood.

Here, we explore the role of AHR activity in CD4+ T cells using EAE. We have demonstrated that deleting *Ahr* from CD4+ T cells increases recovery in EAE in a microbiome-dependent manner. This improved recovery was the result of increased T cell apoptosis after activation in the CNS. While AHR deficiency did not alter the composition of the microbiome, it significantly impacted the production of microbiome-derived metabolites. In particular, AHR deficiency in T cells leads to an increase in bile acids (BA) and a subset of short-chain fatty acids (SCFA) that ultimately impacts T cell viability. Our study demonstrates a novel role for AHR in T lymphocytes as a regulator of the microbiome activity that ultimately influences the outcome of CNS autoimmunity. Our discovery builds the foundation for further work that could lead to a microbiome centric approach to dampen the overactive immune system in MS and related autoimmune disorders.

RESULTS

Gut flora of CD4+ specific *Ahr* knockout mice drives recovery from EAE:

AHR is a transcription factor expressed by immune cells including T cells(*25*). The activity of AHR is modulated by metabolites produced by the microbiota and present in the environment(*15*). Given the emerging role of the microbiome and the well accepted contribution of T cells to MS pathology, AHR is ideally positioned to influence the pathology of CNS autoimmunity. Here we explored the role of AHR in CD4+ T cells in EAE. For this study, we used the previously validated $Cd4^{cre}Ahr^{fl/fl}$ and littermate control $Ahr^{fl/fl}$ mouse strains(*26*). Cohoused adult littermate mice were immunized with myelin oligodendrocyte glycoprotein $(MOG)^{35-55}$ to induce active EAE. The cohoused mice showed no difference in EAE clinical score when *Ahr* expression was removed from CD4+ cells (**Figure 1A, Supplement 1A**; Females **Supplement 1B-C;** Males). Further, we observed no difference in myelin coverage in the spinal cord, as revealed by Luxol Fast Blue staining at the chronic phase (**Figure 1B-C**). To assess the role of AHR driven microbiome changes in EAE, we separated mice by genotype at weaning (3 weeks) and induced EAE between ages 8 and 16 weeks of age. In this condition, while the time of onset and the peak scores of EAE were not impacted, mice lacking *Ahr* expression in T cells presented with a significant recovery when compared to wild type animals (Females; **Figure 1D, Supplement 1D**). Furthermore, the change in recovery does not appear to be driven by sex as it was conserved in both sexes (Males; **Supplement 1E-F**). In agreement with clinical scores, the demyelination of the spinal cords was not different between the two groups at the peak of disease (day 16); however, we noted a significant increase in myelin

coverage at the chronic phase (day 31) in the *Cd4*^{cre}*Ahr*$^{fl/fl}$ animals when compared to the control (**Figures 1E and F**). Together, these data indicate that the lack of *Ahr* expression in CD4+ cells promotes EAE recovery in a microbiome-dependent manner that can be reversed by cohousing.

T cell skewing and activity are unchanged in *Cd4*^{cre}*Ahr*$^{fl/fl}$ mice:

CD4+ T cells are responsible for orchestrating EAE pathology, and defects in these cells have been shown to impact disease outcomes(*27*). Additionally, AHR agonists can modulate T cell skewing in a ligand dependent manner *in vivo*(*28*). Therefore, we have examined T cell skewing capacity and the production of cytokines in *Cd4*^{cre}*Ahr*$^{fl/fl}$ mice. We found that in cohoused mice, the deletion of AHR in T cells did not impact *in vitro* skewing capacity as determined by expression of the main lineage transcription factor by flow cytometry (**Figure 2A-D**) or production of the principle cytokine for each lineage by ELISA (**Figure 2E-H**). Furthermore, there were no differences in the immune cell composition between the knockout and control animals at baseline (**Figure 2I-K**). We also found no differences in pathologic cytokine levels in the spinal cord tissue at the peak of disease as measured by Luminex assay (**Figure 2L-Q**). These findings suggest that CD4 cell intrinsic AHR activity is not necessary for normal T cell development and activity supporting published work indicating that AHR activation of the antigen presenting cell may be more important to T cell subset generation *in vivo*(*29–31*). Further, these data reinforce that the cell intrinsic changes to T cells in *Cd4*^{cre}*Ahr*$^{fl/fl}$ mice are not responsible for EAE recovery.

***Cd4*^{cre}*Ahr*$^{fl/fl}$ mice have fewer T cells in the spinal cord during EAE:**

To determine whether EAE recovery in *Cd4*^{cre}*Ahr*$^{fl/fl}$ was linked to a difference in immune cell number during pathology, we quantified CD45+ immune cells in the spinal cord

tissue using immunohistochemistry at the peak and chronic stages of EAE progression (**Figure 3A-B**). While the quantity of CD45+ cells was equivalent at the peak of the disease, we observed a decrease in the number of CD45+ cells in the *Cd4*^{cre}*Ahr*$^{fl/fl}$ spinal cord compared to controls at the chronic phase (**Figure 3B**). To test if this decrease was due to a reduction in T cells, we next quantified a pan T cell marker, CD3, by immunohistochemistry. We saw no difference in the CD3+ cells in the spinal cord at the peak of disease (**Figure 3C**); however, at the chronic phase, significantly lower CD3+ T cell coverage was observed in the *Cd4*^{cre}*Ahr*$^{fl/fl}$ mice compared to the separately housed littermate controls (**Figure 3D**). We confirmed this outcome using flow cytometry on percoll-isolated immune cells from the spinal cord. At the peak of disease, we again observed no differences in infiltrating T cells (CD4+ or CD8+), T cell subsets (RORgt+, Tbet+ GATA3+ or FoxP3+) or macrophages (CD11b+) (**Figure 3E**). At the chronic phase of disease, we found that the loss of T cells was limited to the CD4+ compartment and not the CD8+ compartment. Of the classic CD4 helper cell subtypes, all trended down in *Cd4*^{cre}*Ahr*$^{fl/fl}$ mice with no one subtype constituting a significant decrease, indicating a pan-CD4+ phenotype, not associated with a specific subtype of CD4+ T cells (**Figure 3F**). Taken together, our data suggest that in separately housed mice, EAE recovery observed in *Cd4*^{cre}*Ahr*$^{fl/fl}$ mice is not due to a difference in cytokine expression or T cell differentiation. Instead, recovery correlates with an overall reduction in CD4+ T cell numbers at the chronic phase of disease and suggests a role for AHR and the microbiome in CD4+ T cell fitness.

Apoptosis of *Ahr* deficient CD4 T cell is microbiome dependent:

We next investigated the mechanism behind the reduced T cell numbers in the spinal cords of *Cd4*^{cre} *Ahr*$^{fl/fl}$ mice during chronic EAE. We performed a gene expression analysis on

whole spinal cord tissues isolated from *Cd4*^{cre}*Ahr*$^{fl/fl}$ and *Ahr*$^{fl/fl}$ at the peak of EAE using a qPCR array composed of 384 genes associated with neuroinflammation. We found that the expression of many genes involved in apoptosis were modulated in the spinal cord tissue of *Cd4*^{cre}*Ahr*$^{fl/fl}$ mice; in particular we noted increased expression of *Fas, GrB, Casp3,* and *Casp9* and decreased expression of the antiapoptotic transcript of *Xiap,* indicating an increase in apoptosis in CD4 specific *Ahr*-deficient mice (**Figure 4A**). We next co-stained the spinal cords for TUNEL and CD3 by immunofluorescence to quantify T cell apoptosis in (**Figure 4B**). While we could detect some apoptotic T cells in the spinal cords of control mice subjected to EAE, CD3+TUNEL+ cell numbers were significantly increased in the spinal cords of *Ahr* deficient animals (closed triangles; **Figure 4C**). We confirmed this observation by quantifying cellular death of isolated immune cells from the spinal cord at the peak of disease using flow cytometry. We observed a significant and specific increase in the percentage of dead CD4+ T cells without change in the percentage of dead CD8+ and myeloid cells between genotypes (**Figure 4D**). To further understand the mechanisms behind these observations, we focused examination on the primary pathogenic subset of CD4+ cells in EAE, the type 17 T helper cell (T_H17)(*32*). To obtain T_H17 cells we isolated naïve CD4+ cells from the lymph nodes and spleen, then cultured the cells in T_H17 differentiation conditions. Similar to the *in vivo* observations, *Cd4*^{cre}*Ahr*$^{fl/fl}$ T_H17 cells have a significant increase in apoptosis after *in vitro* stimulation by anti-CD3 as measured by Annexin V staining compared to littermate controls (**Figure 4E**). Increased T_H17 cell death was only observed in cells isolated from *Cd4*^{cre}*Ahr*$^{fl/fl}$ animals separated at weaning, as T cells isolated from cohoused *Cd4*^{cre}*Ahr*$^{fl/fl}$ mice did not display elevated apoptosis (**Figure 4F**). Taken together, these results support the hypothesis that gut microenvironment may be implicated in the *Ahr*-dependent T cell fitness phenotype. To directly test this hypothesis, we isolated metabolites

(<3kDa) from cecums of separately housed *Cd4*^{cre}*Ahr*$^{fl/fl}$ and *Ahr*$^{fl/fl}$ mice, and added them to *in vitro* skewed T_H17 cells from C57BL6/J mice and analyzed apoptosis by flow cytometry. T_H17 cells exposed to metabolites derived from the gut of *Cd4*^{cre}*Ahr*$^{fl/fl}$ mice had elevated apoptosis compared to cells exposed to metabolites from *Ahr*$^{fl/fl}$ microbiome (**Figure 4G**). We next transferred the microbiome from *Ahr*$^{fl/fl}$ or *Cd4*^{cre}*Ahr*$^{fl/fl}$ donor mice to antibiotics-ablated C57BL6/J recipients followed by EAE induction (**Figure 4H**). Mice that received the microbiota of *Cd4*^{cre}*Ahr*$^{fl/fl}$ donors recovered from EAE better than the mice reconstituted with *Ahr*$^{fl/fl}$ microbiome (**Figure 4I**), paralleling our observations in the donor mice (**Figure 1B**). Collectively, these data demonstrate that exposure to the microbial metabolites from *Cd4*^{cre}*Ahr*$^{fl/fl}$ mice is sufficient to induce early T cell apoptosis and which likely contributes to recovery in EAE.

Taurocholic acid and isovaleric acid induce T_H17 cell apoptosis:

To identify the impact of CD4 cell AHR loss on the gut microenvironment, we began by performing 16S sequencing of DNA isolated from fecal pellets of *Ahr*$^{fl/fl}$ or *Cd4*^{cre}*Ahr*$^{fl/fl}$ mice. Neither cohoused nor separately housed animals saw differences in fecal or cecal microbial compositions (**Supplement 2A-D**). Given the drastic effect of the metabolites prepared from the cecums of *Cd4*^{cre}*Ahr*$^{fl/fl}$ and *Ahr*$^{fl/fl}$ on T cell apoptosis (**Figure 4G**), we next conducted untargeted metabolomics by LC-MS on these preparations (<3kDa). Two-dimensional clustering of the annotated products by revealed distinct clustering of genotypes, indicating significantly different chemical profiles (**Figure 5A**). This difference occurred despite there being no significant difference in the 16S microbial signatures of the cecal contents suggesting that AHR activity in T cells modify the function of the microbiota without altering the composition to a degree that can

be captured by 16S sequencing (**Supplement 2E-F**). Impact analysis of biological pathways identified primary bile acid biosynthesis was the most significantly upregulated pathway with six primary or secondary bile acids significantly increased in the cecal microenvironment of *Cd4*^{cre}*Ahr*$^{fl/fl}$ mice (**Figure 5B, C**). Bile acids are dysregulated systemically with patients with MS and treatment with secondary Bile Acids is sufficient to reduce the severity of EAE(*33*). Bile acid biosynthesis is known to be dependent on the gut microbiota composition(*34*, *35*). Evidence of changes in the secondary bile acid, deoxycholic acid, can be used as a proxy for changes in the microbial activity, as it is a product of bacterial (rather than mammalian) metabolism(*36*). Of the changed bile acids, taurocholic acid was the most highly upregulated with over a 10-fold increase in *Cd4*^{cre}*Ahr*$^{fl/fl}$ compared to control mice (**Figure 5C**). When used to treat C57BL6/J derived T_H17 cells *in vitro,* taurocholic acid was sufficient to drive apoptosis (**Figure 5D**). This is in support of recent work showing that bile acid receptor agonists reduce T cell activation and suppress EAE (*37*, *38*). In addition to changes in bile acids, alanine, aspartate, and glutamate metabolism were also upregulated, whereas purine metabolism and tryptophan metabolism were downregulated in *Cd4*^{cre}*Ahr*$^{fl/fl}$ mice. As short chain fatty acids (SCFAs) have been reported to impact the viability of inflammatory T cell and cannot be captured through untargeted metabolomics, we next performed targeted SCFA metabolomics (*39*, *40*). Isovaleric acid was the only SCFA with a significantly higher abundance in the *Cd4*^{cre}*Ahr*$^{fl/fl}$ cecums compared to controls (**Figure 5E**), and was sufficient to drive apoptosis when administered to *in vitro* skewed T_H17 cells (**Figure 5F**). We also tested valeric acid and hexanoic acid (similar in size and structure to isovaleric acid), as we noted trends in their increase in the *Cd4*^{cre}*Ahr*$^{fl/fl}$ cecums. We found that hexanoic acid, but not valeric acid can also induce TH17 apoptosis (**Figure 5 E-F**). Collectively, our data suggest that the combined effects

of the cecal milieu of *Cd4*^{cre}*Ahr*$^{fl/fl}$ mice could induce lasting changes in T cell fitness, ultimately resulting in recovery from paralysis in EAE.

DISCUSSION

Here we demonstrate that the deletion of the aryl hydrocarbon receptor (AHR) in CD4+ cells can promote recovery in chronic EAE while having no impact on the onset nor the initial magnitude of the disease. We further show that this phenotype is dependent on the microbiome, as cohousing littermate *Cd4*^{cre}*Ahr*$^{fl/fl}$ and *Ahr*$^{fl/fl}$ mice abrogates recovery in EAE. These data are in support of previous work in similar models has shown no difference in EAE recovery after T cell-specific *Ahr* deletion(*41*). At the mechanistic level, our data suggest that specific metabolites elevated in the cecum of *Cd4*^{cre}*Ahr*$^{fl/fl}$ mice reduce T cell fitness and viability. In particular, the cecal environment of *Cd4*^{cre}*Ahr*$^{fl/fl}$ animals is characterized by high levels of isovaleric acid and taurocholic acid, which induce T cell apoptosis *in vitro,* suggesting a likely mechanism for EAE recovery.

AHR activity can regulate autoimmunity via natural killer (NK) cells(*42*), macrophages(*43*), dendritic cells(*44*), and T cells(*28*, *45*, *46*)-all contributors to EAE pathogenesis. AHR activation is a known regulator of T cell differentiation and inflammatory to regulatory T cell ratios. Importantly, T cell activity is dependent on the specific ligand activation with some promoting a pro-inflammatory environment, and others having the opposite effect(*28*). It has been postulated that T cell intrinsic AHR activity is necessary for differentiation but several groups have shown that AHR antagonists do not have a cell intrinsic effect on T cell differentiation leaving remaining questions in the field(*47*). Here we demonstrate that T ceel specific AHR expression is not necessary for the differentiation of T cells *in vitro* supporting the hypothesis that the AHR activity in antigen presenting cell is the

necessary factor influencing T cell differentiation *in vivo*(*29–31*). Beyond T cells, AHR activation in glial cells regulates the pathogenic effects of microglia and astrocytes in EAE via changed cytokine production (*48*, *49*). AHR's ubiquitous expression in barrier tissues coupled with its complex ligand binding profile warrants further study of AHR function in autoimmunity. We have identified that the changes of the luminal microenvironment of the small intestine resulting from *Ahr* knockout in CD4+ cells lead to decreased post-activation lifespan in T cells; however, the impact of these changes on other cell types and other models of autoimmunity have yet to be determined. Bile acids, SCFAs, and other small molecules we identified can move into circulation and some can gain entry into the central nervous system by crossing the blood brain barrier(*50*). There are likely systemic effects that have yet to be described. For example, our data suggest that significant remyelination is taking place in the chronic phase of EAE in CD4 specific *Ahr* knockout animals. Given the described impact of the microbiome and SCFA on myelination(*51*, *52*), it would be critical to test if the metabolic signature generated by the lack of *Ahr* in T cells can influence oligodendrocyte generation.

The data presented here support an interdependence between T cells and the microbiome that is AHR dependent. However, it remains to be understood how T cells can modulate the metabolic signature of the cecum. We hypothesize that *Ahr* deletion in T cells may lead to modulation of IgA secretion by B cells(*53*, *54*). IgA is the primary mechanism by which the adaptive immune system can directly modulate mucosal microbial communities(*53*). An alternative hypothesis is that immune cell activity is modulating antimicrobial peptide release indirectly through communication with Paneth cells(*55*, *56*). Most work on these systems thus far has focused on models of severe microbiome dysbiosis. Less is known about the subtler changes in the microbiome subject to homeostatic regulation. Therefore, the mechanism by

which the adaptive immune system can interface with the microbiota is of great interest for understanding the basis of autoimmune disorders.

The changes in bile acids as a result of *Ahr* knockout in the T cells is striking. Bile acids are produced by the host for digestion and are normally reabsorbed by transporters (primary) or passively (primary conjugated) in the ileum while secondary bile acids are not as easily absorbed (*36*). There is an increase in conjugated bile acids in *Ahr* knockout mice, but lower levels of secondary bile acids. This is the inverse of patients with MS indicating that there may be a causative connection in both patients and mice with EAE(*33*). Further studies are needed to understand which step of this pathway: production, conversion or absorption are influenced by the gut flora and/or the T cells. Our results support the existing work in synthetic bile acid receptor agonists that T cell fitness and activity can be mediated by bile acid receptor activation(*37*, *38*). This evidence that bile acids can have a direct influence on T cell function warrants further study in the context of autoimmune diseases.

Microbiome-modulated immune responses become particularly important in patients with chronic and relapsing autoimmune conditions like MS(*57–61*). We have described a novel function for the environmental sensor AHR in T cells as a regulator of the gut microenvironment. As we further understand the complexities of harnessing the gut microbiome, we predict tools for controlling host-derived microbe modulation will be a new frontier for therapeutics. Our work is an important step in the discovery of a targetable endogenous modulator of the microbiome opens a potential new therapeutic avenue for MS patients.

MATERIALS AND METHODS

Experimental Design The objective of these studies was to understand the role of CD4 specific AHR activity in EAE. Immunophenotyping and characterization of the mice occurred in

cohoused mice to determine the purely genetic differences. Once no major changes were discovered in the *Ahr* knockout mice, we began to separately house them based on genotype. This allowed us to examine the microbiome-dependent features of autoimmunity and the development of further hypotheses. Sample sizes were determined by power analysis. The final desired n was divided by two and included for each experiment. In this way, we have two independent experiments resulting in appropriate power. Except where otherwise stated, all experiments were conducted twice independently. Data collection for all EAE experiments ended at 30 days- the time point at which we have defined as chronic stage. All experiments were conducted on age- and sex- matched animals. Histological analysis was conducted by a blinded investigator. EAE scores are reported as the average of two blinded investigators to account for interrater variability. Statistical outliers are not included in analysis or figures.

Mice AHR$^{tm3.1Bra}$/J(Ahr^{fx}) (#006203), B6.Cg-Tg(Cd4-cre)1Cwi/BfluJ (CD4Cre) (#022071), and C57BL/6J (#000664) mice were purchased from Jackson Laboratories. Mice were bred in-house with a 12-hour light/dark schedule. Cohoused mice were housed with their littermates of the same sex from birth. Separately housed mice were separated at weaning (3 weeks) based on presence of Cre. Litters born within 4 days of each other were housed together to achieve 2-5 mice per cage. All procedures were approved by the University of Virginia ACUC (protocol #1918).

Experimental autoimmune encephalomyelitis EAE was induced in both male and female mice between 8 and 12 weeks of age. MOG_{35-55} peptide (100µg, CSBio, CS0681) was emulsified in complete Freund's adjuvant containing *Mycobacterium tuberculosis* (1mg/mL, Sigma, F5881; M. tuberculosis (BD 231141) added to final concentration of 4mg/mL) and was injected subcutaneously (100 µl volume) at the base of the tail. Pertussis toxin (200 ng, List

Biologicals, 180) was administered i.p. on the day of and 1 day after MOG immunization. Mice were scored daily by two blinded evaluators using the following scale: 0-no clinical disease, 1-limp tail, 2-hindlimb incoordination, 3-hindlimb weakness, 4-hindlimb paralysis, 5-moribund. As is standard practice, animals who did not develop any signs of EAE were excluded from analysis-total incidence is reported in the supplement.

Immunohistochemistry and Fluorescent Microscopy Spinal cords were prepared as previously described(*62*). Slides were deparaffinized using xylenes and an ethanol gradient. IHC antibodies used were anti-CD3 (Dako; A0452) at 1:200 dilution and anti-CD45 (BD Biosciences; 550539) at 1:80 dilution. Adjacent sections were stained with Luxol Fast Blue and Hemtolxylin and Eosin for demyelinating plaques. Images were taken using an EVOS Cryosections (30µm) were stained with anti-CD3 (eBioscience; 50-0032-82) or isotype control (Fisher Scientific; 14-0032-82) as previously described(*62*). A positive control slide was treated with DNAse (3000U/mL). After staining, sections were fixed with paraformaldehyde for 15 minutes at room temperature. Sections were washed two times in PBS followed by proteinase K (200ug/mL in PBS) treatment for 10 minutes at room temperature. Sections were washed twice with PBS and incubated with TUNEL reaction mixture (Roche; 12156792910) for 60 minutes at 37 ºC in a humidified chamber. Sections were washed three times in PBS and mounted using Prolong Gold Anti-Fade Reagent (Life Technologies). Slides were imaged with a Leica TCS SP8 confocal microscope. All images were analyzed with ImageJ. Histological analysis was performed by a blinded evaluator.

Enzyme-linked immunosorbent Assay ELISA for IFNγ, IL-4, IL-17, and IL-10 were performed as previously described(*63*). Antibodies used were as follows: anti-IFNγ (BioLegend; 517902), biotin labeled anti-INFγ (BioLegend; 505704), anti-IL-4 (Thermo Fisher; 14-7041-85),

biotin labeled anti-IL-4 (Thermo Fisher; 13-7042-85), anti-IL-17 (eBioscience; 14-7175-85), biotin labeled anti-IL-17(eBioscience; 13-7177-85), anti-IL-10 (BioLegend; 505002), biotin labeled anti-IL-10 (BioLegend; 505004).

RNA Extraction and Quantitative PCR Whole spinal cords were homogenized using a dounce homogenizer and RNA was extracted using the Bioline Isolate II RNA mini kit as per manufacture's protocol (BIO-52073). RNA was quantified with a Biotek Epoch Microplate Spectrophotometer. Normalized RNA was reverse transcribed to cDNA with either the Bioline SensiFast cDNA Synthesis Kit (BIO-65054). The Bio-Rad PrimePCR plate was used per manufacturer's instructions (Demyelinating Diseases Tier 1-4 M384; 10038953). Results were analyzed with the relative quantity (ΔΔCq) method.

Isolation and Preparation T cells Mesenteric, inguinal, axial, and brachial lymph nodes plus the spleen were dissected from the mice after CO_2 euthanasia. They were then dissociated through sterile 70 μm filters and lysed with ACK lysis buffer (Quality Biological, 118-156-101). Naïve CD4+ T cells were then sorted using an EasySep Mouse CD4+ T cell Isolation Kit (Stem Cell Technologies, #19852). The cells were plated at $1x10^6$ cells/mL in skew media as previously described(*64*).

Apoptosis Assay Skewed T cells were plated at $1x10^6$ cells/mL in 48 well plates coated with anti-CD3. After 24 hours, cells were stained with Ghost Live Dead (Tonbo Biosciences; 13-0870), Annexin 5 (Fisher Scientific; BDB556420) per manufacturer's instructions (Annexin V, fixed using the FoxP3 permeabilization, fixation kit (eBioscience; 00-5523-00), and stained with RORgt PE. Results were gated on singlets, RORgt+, and Annexin 5+, L/D negative.

Isolation of Cecal Contents For both metabolomics and *in vitro* analysis, the <3kDa fraction of the cecal contents were isolated. Cecal contents were extracted from the mice and

suspended in 1mL of IMDM by vortexing. These were then sequentially filtered (70 µm, 40 µm, .22 µm, <50, <3 kDa) to remove insoluble materials and bacteria and macromolecules with a molecular weight > 3kDa. Preparations were used immediately or flash frozen at -80C for up to 3 weeks.

Spinal Cord dissociation Spinal cords were collected in 2.5 mL ice cold HBSS (Gibco, 14025134). Equal amounts of 4mg/mL collagenase 4 (Worthington; LS002139) with 50U/mL DNase (Worthington, LS002139) were added and samples were shaken three times at 37ºC for 15 minutes, triturating in between. Spinal cords were strained through a 70mm filter into 10mL DMEM (Gibco, 11965-092) with 10% FBS (R&D Systems; S12450H). Centrifuge at 260 g for 8 minutes. Resuspend the pellet in a 15mL tube in 12 mL of Percoll (GE Healthcare, 17-0891-01). Centrifuge at 650g for 25 min without brake. The myelin layer and supernatant were aspirated and the pellet was resuspended in 2mL of FACS buffer.

Microbiome Transfer Female C57BL6/J mice were given drinking water containing 1g/L Ampicillin (Sigma-Aldrich; A8351-25G), 1g/L Neomycin (Sigma-Aldrich; N6386-25G), 1g/L Metronidazol (Sigma-Aldrich; M1547-25G), 500mg/mL Vancomycin (Sigma-Aldrich; V1130-5G), and 8mg/mL Splenda for two weeks. Mice were then orally gavaged with fresh filtered (40µm) cecal contents from pooled donor animals on day 0, day 2, and day 4 after removal from antibiotics. On the day of antibiotics withdrawal, a naïve microbiome donor animal was added to the cage and remained for the duration of the experiment. Mice waited two weeks for microbiome equilibrium before they underwent EAE induction.

Flow Cytometry Single cell suspensions were incubated with Fc Block CD16/32 (Invitrogen, 14-0161-85). The cells were then incubated with a 1:200 dilution of antibody for surface stains and A Live/Dead Ghost Dye Violet 510 (Tonbo Biosciences; 13-0870). Surface

antibodies: 488-conjugated CD8 (Invitrogen; 53-008182), APCe780-conjugated TCRβ (Invitrogen; 47-5961-82), e450-conjugated CD4 (Invitrogen; 48-0042-820), 488 conjugated-CD11b (Invitrogen; 53-0112-82), and APC-conjugated CD45.2 (Biolegend; 109813). For transcription factor staining, the eBioscience FoxP3/Transcription Factor Staining Kit (00-5523-00) was used per manufacturer's instructions with intracellular antibodies: PE-conjugated RORγT (Invitrogen; 12-6981-82), PE-Cy7- conjugated FoxP3 (Invitrogen; 25-5773-82), PE-conjugated GATA3 (Invitrogen; 12-9966-42), PE-Cy7-conjugated Tbet (Biolegend; 644824). OneComp eBeads (Thermo Fisher Scientific, 01-111-42) were used for color controls. Flow cytometry was performed using a Beckman Coulter Gallios flow cytometer and data were analyzed with FlowJo software v10.7.1.

LC-MS Untargeted Metabolomics was performed by Creative Proteomics. Cecal samples (<3kDa) were prepared and concentrated as before as described before. Samples were thawed and lyophilized, 200uL of 80% methanol was added. Samples were vortexed and then sonicated for 30 minutes at 4 ºC. Samples were kept at -20 for 1 h, vortexed for 30ss and kept at 4 ºC for 15min until they were centrifuged at 12000 rpm at 4 ºC for 15 min. 100ul of the supernatant and 2.5ul of DL-o-Chlorophenylalanine were used for LC-MS analysis. Separation is performed by Ultimate 3000 LC combined with Q Exactive MS (Thermo) and screened with ESI-MS. The LC system is comprised of ACQUITY UPLC HSS T3 (100×2.1mm×1.8 μm) with Ultimate 3000 LC. The mobile phase is composed of solvent A (0.05% formic acid water) and solvent B (acetonitrile) with a gradient elution (0-1.0 min, 5%B; 1.0-12.0 min, 5%-95%B; 12.0-13.5 min, 95%B; 13.5-13.6 min, 95%-5%B; 13.6-16.0 min, 5%B). The flow rate of the mobile phase is 0.3 mL·min-1. The column temperature is maintained at 40°C, and the sample manager temperature is set at 4°C. Mass spectrometry parameters in ESI+ and ESI- mode are listed as follows:

ESI+: Heater Temp 300 °C; Sheath Gas Flow rate, 45arb; Aux Gas Flow Rate, 15arb; Sweep Gas Flow Rate, 1arb; spray voltage, 3.0KV; Capillary Temp, 350 °C; S-Lens RF Level, 30%. ESI-: Heater Temp 300 °C, Sheath Gas Flow rate, 45arb; Aux Gas Flow Rate, 15arb; Sweep Gas Flow Rate, 1arb; spray voltage, 3.2KV; Capillary Temp,350 °C; S-Lens RF Level,60%.

LC-MS Data Processing LC-MS data was processed using R studio. Analysis was conducted using POMA Shiny version 1.4.0(*65*). In short, we removed features with more than 20% missing values, normalized with log scaling and then completed sparse partial least squares discriminate analysis (sPLS-DA). Top ranked products were utilized in MetaMapp(*66*, *67*) analysis to produce a web of chemically and biologically related compounds. Finally, the top ranked products were also inputted into Metaboanalyst to complete pathway enrichment and determine mouse KEGG terms.

16S Sequencing Data Processing 16S Sequencing was conducted at Microbiome Insights (Cohoused Feces), ZymoBIOMICS (Separately Housed Cecum), and at the University of Virginia Genomics Core (Separately housed Feces). Initial sequence data was analyzed using the latest version of Quantitative Insights Into Microbial Ecology 2 (Qiime2 v2021.11)(*68*). Demultiplexed paired-end sequence reads were preprocessed using DADA2(*69*). The first 20 base pairs were trimmed from forward and reverse reads before they were merged to remove adaptors. Taxonomy was assigned to Amplicon Sequence Variants (ASVs) using a Naïve Bayes classifier trained on full length 16S sequences from the latest Greengenes16S database (13_8) clustered at 99% sequence similarity. Samples were rarified before core diversity analysis. Rarefied sampling depth was 16000 for cecal contents, 30000 for separately housed fecal contents, and 10,411 for cohoused fecal contents. Core diversity metrics were analyzed,

including number of ASVs. Nonmetric multidimensional scaling was performed in RStudio using the phyloseq package(*70*).

Statistical Analysis Unless otherwise noted, all statistical tests were run on Graph Pad Prism 9 Version 9.1.0. Statistical tests and p-values for each comparison are listed in the figure legends or in the supplementary report. In the figure legends, n denotes the total number of animals displayed in the figure used in analysis. In the figure legends, N denotes the total number of replicates that were completed for the given experiment. Testing level of α=0.05 was used throughout.

Supplementary Materials

Figure S1. Separately housed *Cd4*^{cre}*Ahr*$^{fl/fl}$ recover from EAE phase.

Figure S2. Only subtle microbiota population changes in *Cd4*^{cre}*Ahr*$^{fl/fl}$ mice.

Data S1. Statistical report for all data presented in the manuscript.

Data S2. Raw Data files from Negative ion mode LC-MS corresponding to Figure 5 A-C.

Data S3. Raw Data files from Positive ion mode LC-MS corresponding to Figure 5 A-C.

References and Notes

1. A. Compston, A. Coles, Multiple sclerosis. *Lancet*. **372** (2008), pp. 1502–1517.
2. S. Miyake, S. Kim, W. Suda, K. Oshima, M. Nakamura, T. Matsuoka, N. Chihara, A. Tomita, W. Sato, S. W. Kim, H. Morita, M. Hattori, T. Yamamura, Dysbiosis in the gut microbiota of patients with multiple sclerosis, with a striking depletion of species belonging to clostridia XIVa and IV clusters. *PLoS One*. **10** (2015), doi:10.1371/journal.pone.0137429.
3. G. Aaen, A. Belman, L. Benson, C. Casper, T. Chitnis, M. Gorman, Y. Harris, L. Krupp,

T. E. Lotze, S. Lulu, J. Ness, C. Olsen, E. Roan, M. Rodriguez, J. Rose, T. C. Simmons, Jan-Mendelt Tillema, W. Weber, B. Weinstock-Guttman, H. Tremlett, D. W. Fadrosh, A. A. Faruqi, J. Hart, S. Roalstad, J. Graves, C. M. Spencer, S. V. Lynch, S. S. Zamvil, E. Waubant, Associations between the gut microbiota and host immune markers in pediatric multiple sclerosis and controls. *BMC Neurol.* **16** (2016), doi:10.1186/S12883-016-0703-3.

4. J. Chen, N. Chia, K. R. Kalari, J. Z. Yao, M. Novotna, M. M. P. Soldan, D. H. Luckey, E. V. Marietta, P. R. Jeraldo, X. Chen, B. G. Weinshenker, M. Rodriguez, O. H. Kantarci, H. Nelson, J. A. Murray, A. K. Mangalam, Multiple sclerosis patients have a distinct gut microbiota compared to healthy controls. *Sci. Rep.* **6** (2016), doi:10.1038/SREP28484.

5. S. Jangi, R. Gandhi, L. M. Cox, N. Li, F. Von Glehn, R. Yan, B. Patel, M. A. Mazzola, S. Liu, B. L. Glanz, S. Cook, S. Tankou, F. Stuart, K. Melo, P. Nejad, K. Smith, B. D. Topçuolu, J. Holden, P. Kivisäkk, T. Chitnis, P. L. De Jager, F. J. Quintana, G. K. Gerber, L. Bry, H. L. Weiner, Alterations of the human gut microbiome in multiple sclerosis. *Nat. Commun. 2016 71*. **7**, 1–11 (2016).

6. M. K. Boziki, E. Kesidou, P. Theotokis, A. F. A. Mentis, E. Karafoulidou, M. Melnikov, A. Sviridova, V. Rogovski, A. Boyko, N. Grigoriadis, Microbiome in multiple sclerosis; where are we, what we know and do not know. *Brain Sci.* **10** (2020), , doi:10.3390/brainsci10040234.

7. A. Merchak, A. Gaultier, Microbial metabolites and immune regulation: New targets for major depressive disorder. *Brain, Behav. Immun. - Heal.* **9**, 100169 (2020).

8. D. J. Levinthal, A. Rahman, S. Nusrat, M. O'Leary, R. Heyman, K. Bielefeldt, Adding to the Burden: Gastrointestinal Symptoms and Syndromes in Multiple Sclerosis. *Mult. Scler. Int.* **2013**, 1–9 (2013).

9. L. M. Cox, A. H. Maghzi, S. Liu, S. K. Tankou, F. H. Dhang, V. Willocq, A. Song, C. Wasén, S. Tauhid, R. Chu, M. C. Anderson, P. L. De Jager, M. Polgar-Turcsanyi, B. C. Healy, B. I. Glanz, R. Bakshi, T. Chitnis, H. L. Weiner, Gut Microbiome in Progressive Multiple Sclerosis (2021), doi:10.1002/ana.26084.

10. K. Berer, L. A. Gerdes, E. Cekanaviciute, X. Jia, L. Xiao, Z. Xia, C. Liu, L. Klotz, U. Stauffer, S. E. Baranzini, T. Kümpfel, R. Hohlfeld, G. Krishnamoorthy, H. Wekerle, Gut microbiota from multiple sclerosis patients enables spontaneous autoimmune encephalomyelitis in mice. *Proc. Natl. Acad. Sci. U. S. A.* **114**, 10719–10724 (2017).

11. S. Jangi, R. Gandhi, L. M. Cox, N. Li, F. Von Glehn, R. Yan, B. Patel, M. A. Mazzola, S. Liu, B. L. Glanz, S. Cook, S. Tankou, F. Stuart, K. Melo, P. Nejad, K. Smith, B. D. Topçuolu, J. Holden, P. Kivisäkk, T. Chitnis, P. L. De Jager, F. J. Quintana, G. K. Gerber, L. Bry, H. L. Weiner, Alterations of the human gut microbiome in multiple sclerosis. *Nat. Commun.* **7** (2016), doi:10.1038/ncomms12015.

12. K. Berer, M. Mues, M. Koutrolos, Z. AlRasbi, M. Boziki, C. Johner, H. Wekerle, G. Krishnamoorthy, Commensal microbiota and myelin autoantigen cooperate to trigger autoimmune demyelination. *Nature*. **479**, 538–541 (2011).

13. D. M. Johanson, J. E. Goertz, I. A. Marin, J. Costello, C. C. Overall, A. Gaultier, Experimental autoimmune encephalomyelitis is associated with changes of the microbiota composition in the gastrointestinal tract. *Sci. Rep.* **10** (2020), doi:10.1038/s41598-020-

72197-y.

14. A. Barroso, J. V. Mahler, P. H. Fonseca-Castro, F. J. Quintana, The aryl hydrocarbon receptor and the gutâ€"brain axis. *Cell. Mol. Immunol.*, doi:10.1038/s41423-020-00585-5.

15. T. D. Hubbard, I. A. Murray, W. H. Bisson, T. S. Lahoti, K. Gowda, S. G. Amin, A. D. Patterson, G. H. Perdew, Adaptation of the human aryl hydrocarbon receptor to sense microbiota-derived indoles. *Sci. Rep.* **5** (2015), doi:10.1038/srep12689.

16. U.-H. Jin, S.-O. Lee, G. Sridharan, K. Lee, L. A. Davidson, A. Jayaraman, R. S. Chapkin, R. Alaniz, S. Safe, Microbiome-Derived Tryptophan Metabolites and Their Aryl Hydrocarbon Receptor-Dependent Agonist and Antagonist Activities. *Mol. Pharmacol.* **85** (2014), doi:10.1124/mol.113.091165.

17. M. S. Denison, S. C. Faber, And now for something completely different: Diversity in ligand-dependent activation of Ah receptor responses. *Curr. Opin. Toxicol.* **2** (2017), , doi:10.1016/j.cotox.2017.01.006.

18. M. Ott, E. Avendanõ-Guzmán, E. Ullrich, C. Dreyer, J. Strauss, M. Harden, M. Schön, M. P. Schön, G. Bernhardt, C. Stadelmann, C. Wegner, W. Brück, S. Nessler, Laquinimod, a prototypic quinoline-3-carboxamide and aryl hydrocarbon receptor agonist, utilizes a CD155-mediated natural killer/dendritic cell interaction to suppress CNS autoimmunity. *J. Neuroinflammation*. **16**, 1–14 (2019).

19. J. Kaye, V. Piryatinsky, T. Birnberg, T. Hingaly, E. Raymond, R. Kashi, E. Amit-Romach, I. S. Caballero, F. Towfic, M. A. Ator, E. Rubinstein, D. Laifenfeld, A. Orbach, D. Shinar, Y. Marantz, I. Grossman, V. Knappertz, M. R. Hayden, R. Laufer, Laquinimod arrests experimental autoimmune encephalomyelitis by activating the aryl hydrocarbon receptor. *Proc. Natl. Acad. Sci. U. S. A.* **113**, E6145–E6152 (2016).

20. A. Korecka, A. Dona, S. Lahiri, A. J. Tett, M. Al-Asmakh, V. Braniste, R. D'Arienzo, A. Abbaspour, N. Reichardt, Y. Fujii-Kuriyama, J. Rafter, A. Narbad, E. Holmes, J. Nicholson, V. Arulampalam, S. Pettersson, Bidirectional communication between the Aryl hydrocarbon Receptor (AhR) and the microbiome tunes host metabolism. *npj Biofilms Microbiomes 2016 21*. **2**, 1–10 (2016).

21. F. Yang, J. A. A. DeLuca, R. Menon, E. Garcia-Vilarato, E. Callaway, K. K. Landrock, K. Lee, S. H. Safe, R. S. Chapkin, C. D. Allred, A. Jayaraman, Effect of diet and intestinal AhR expression on fecal microbiome and metabolomic profiles. *Microb. Cell Fact.* **19**, 1–18 (2020).

22. I. A. Murray, R. G. Nichols, L. Zhang, A. D. Patterson, G. H. Perdew, Expression of the aryl hydrocarbon receptor contributes to the establishment of intestinal microbial community structure in mice. *Sci. Rep.* **6** (2016), doi:10.1038/srep33969.

23. R. R. Fling, T. R. Zacharewski, Aryl hydrocarbon receptor (Ahr) activation by 2,3,7,8-tetrachlorodibenzo-p-dioxin (tcdd) dose-dependently shifts the gut microbiome consistent with the progression of non-alcoholic fatty liver disease. *Int. J. Mol. Sci.* **22** (2021), doi:10.3390/IJMS222212431/S1.

24. O. A. Abdulla, W. Neamah, M. Sultan, H. K. Alghetaa, N. Singh, P. B. Busbee, M. Nagarkatti, P. Nagarkatti, The Ability of AhR Ligands to Attenuate Delayed Type Hypersensitivity Reaction Is Associated With Alterations in the Gut Microbiota. *Front.*

Immunol. **12**, 2505 (2021).

25. T. D. Hubbard, I. A. Murray, W. H. Bisson, A. P. Sullivan, A. Sebastian, G. H. Perry, N. G. Jablonski, G. H. Perdew, Divergent Ah Receptor Ligand Selectivity during Hominin Evolution. *Mol. Biol. Evol.* **33** (2016), doi:10.1093/molbev/msw143.

26. C. Rivet-Noor, A. Merchak, S. Li, R. Beiter, S. Lee, J. Thomas, A. Fernández-Castañeda, J. Shin, A. Gaultier, Stress-Induced Despair Behavior Develops Independently of the AHR-RORgt Axis in CD4+ cells. *Res. Sq.* (2022), doi:10.21203/RS.3.RS-1181536/V1.

27. F. C. Kurschus, T cell mediated pathogenesis in EAE: Molecular mechanisms. *Biomed. J.* **38**, 183–193 (2015).

28. A. K. Ehrlich, J. M. Pennington, W. H. Bisson, S. K. Kolluri, N. I. Kerkvliet, TCDD, FICZ, and Other High Affinity AhR Ligands Dose-Dependently Determine the Fate of CD4+ T Cell Differentiation. *Toxicol. Sci.* **161**, 310–320 (2018).

29. C. H. Hong, S. H. Lin, B. E. Clausen, C. H. Lee, Selective AhR knockout in langerin-expressing cells abates Langerhans cells and polarizes Th2/Tr1 in epicutaneous protein sensitization. *Proc. Natl. Acad. Sci. U. S. A.* **117**, 12980–12990 (2020).

30. J. H. Duarte, P. Di Meglio, K. Hirota, H. Ahlfors, B. Stockinger, Differential Influences of the Aryl Hydrocarbon Receptor on Th17 Mediated Responses in vitro and in vivo. *PLoS One*. **8**, e79819 (2013).

31. F. J. Quintana, G. Murugaiyan, M. F. Farez, M. Mitsdoerffer, A. M. Tukpah, E. J. Burns, H. L. Weiner, An endogenous aryl hydrocarbon receptor ligand acts on dendritic cells and T cells to suppress experimental autoimmune encephalomyelitis. *Proc. Natl. Acad. Sci. U. S. A.* **107**, 20768–20773 (2010).

32. C. C. Angelou, A. C. Wells, J. Vijayaraghavan, C. E. Dougan, R. Lawlor, E. Iverson, V. Lazarevic, M. Y. Kimura, S. R. Peyton, L. M. Minter, B. A. Osborne, E. L. Pobezinskaya, L. A. Pobezinsky, Differentiation of Pathogenic Th17 Cells Is Negatively Regulated by Let-7 MicroRNAs in a Mouse Model of Multiple Sclerosis. *Front. Immunol.* **10**, 3125 (2020).

33. P. Bhargava, M. D. Smith, L. Mische, E. Harrington, K. C. Fitzgerald, K. Martin, S. Kim, A. A. Reyes, J. Gonzalez-Cardona, C. Volsko, A. Tripathi, S. Singh, K. Varanasi, H. N. Lord, K. Meyers, M. Taylor, M. Gharagozloo, E. S. Sotirchos, B. Nourbakhsh, R. Dutta, E. M. Mowry, E. Waubant, P. A. Calabresi, Bile acid metabolism is altered in multiple sclerosis and supplementation ameliorates neuroinflammation. *J. Clin. Invest.* **130**, 3467 (2020).

34. S. I. Sayin, A. Wahlström, J. Felin, S. Jäntti, H. U. Marschall, K. Bamberg, B. Angelin, T. Hyötyläinen, M. Orešič, F. Bäckhed, Gut microbiota regulates bile acid metabolism by reducing the levels of tauro-beta-muricholic acid, a naturally occurring FXR antagonist. *Cell Metab.* **17**, 225–235 (2013).

35. C. Ma, M. Han, B. Heinrich, Q. Fu, Q. Zhang, M. Sandhu, D. Agdashian, M. Terabe, J. A. Berzofsky, V. Fako, T. Ritz, T. Longerich, C. M. Theriot, J. A. McCulloch, S. Roy, W. Yuan, V. Thovarai, S. K. Sen, M. Ruchirawat, F. Korangy, X. W. Wang, G. Trinchieri, T. F. Greten, Gut microbiome–mediated bile acid metabolism regulates liver cancer via NKT cells. *Science (80-.).* **360** (2018),

doi:10.1126/SCIENCE.AAN5931/SUPPL_FILE/AAN5931_MA_SM.PDF.

36. T. M. Šarenac, M. Mikov, Bile acid synthesis: From nature to the chemical modification and synthesis and their applications as drugs and nutrients. *Front. Pharmacol.* **9**, 939 (2018).

37. N. D. Lewis, L. A. Patnaude, J. Pelletier, D. J. Souza, S. M. Lukas, F. J. King, J. D. Hill, D. E. Stefanopoulos, K. Ryan, S. Desai, D. Skow, S. G. Kauschke, A. Broermann, D. Kuzmich, C. Harcken, E. R. Hickey, L. K. Modis, A GPBAR1 (TGR5) Small Molecule Agonist Shows Specific Inhibitory Effects on Myeloid Cell Activation In Vitro and Reduces Experimental Autoimmune Encephalitis (EAE) In Vivo. *PLoS One*. **9**, e100883 (2014).

38. P. P. Ho, L. Steinman, Obeticholic acid, a synthetic bile acid agonist of the farnesoid X receptor, attenuates experimental autoimmune encephalomyelitis. *Proc. Natl. Acad. Sci. U. S. A.* **113**, 1600 (2016).

39. Z. MA, S. N, M. PM, T. M, G. V, W. JL, S. H, R. KD, M. DH, L. K, Butyrate suppresses colonic inflammation through HDAC1-dependent Fas upregulation and Fas-mediated apoptosis of T cells. *Am. J. Physiol. Gastrointest. Liver Physiol.* **302** (2012), doi:10.1152/AJPGI.00543.2011.

40. T. Kurita-Ochiai, K. Ochiai, K. Fukushima, Butyric Acid-Induced T-Cell Apoptosis Is Mediated by Caspase-8 and -9 Activation in a Fas-Independent Manner. *Clin. Diagn. Lab. Immunol.* **8**, 325 (2001).

41. J. H. Duarte, P. Di Meglio, K. Hirota, H. Ahlfors, B. Stockinger, Differential Influences of the Aryl Hydrocarbon Receptor on Th17 Mediated Responses in vitro and in vivo (2013), doi:10.1371/journal.pone.0079819.

42. J. H. Shin, U. Y. Moreno-Nieves, L. H. Zhang, C. Chen, A. L. Dixon, M. H. Linde, E. M. Mace, J. B. Sunwoo, AHR Regulates NK Cell Migration via ASB2–Mediated Ubiquitination of Filamin A. *Front. Immunol.* **12**, 94 (2021).

43. C. Wang, Z. Ye, A. Kijlstra, Y. Zhou, P. Yang, Activation of the aryl hydrocarbon receptor affects activation and function of human monocyte-derived dendritic cells. *Clin. Exp. Immunol.* **177**, 521–530 (2014).

44. F. J. Quintana, G. Murugaiyan, M. F. Farez, M. Mitsdoerffer, A.-M. Tukpah, E. J. Burns, H. L. Weiner, An endogenous aryl hydrocarbon receptor ligand acts on dendritic cells and T cells to suppress experimental autoimmune encephalomyelitis, doi:10.1073/pnas.1009201107.

45. F. J. Quintana, G. Murugaiyan, M. F. Farez, M. Mitsdoerffer, A. M. Tukpah, E. J. Burns, H. L. Weiner, An endogenous aryl hydrocarbon receptor ligand acts on dendritic cells and T cells to suppress experimental autoimmune encephalomyelitis. *Proc. Natl. Acad. Sci. U. S. A.* **107**, 20768–20773 (2010).

46. Y. Lee, A. Awasthi, N. Yosef, F. J. Quintana, S. Xiao, A. Peters, C. Wu, M. Kleinewietfeld, S. Kunder, D. A. Hafler, R. A. Sobel, A. Regev, V. K. Kuchroo, Induction and molecular signature of pathogenic T H 17 cells. *Nat. Immunol.* (2012), doi:10.1038/ni.2416.

47. J. P. McAleer, J. Fan, B. Roar, D. A. Primerano, J. Denvir, Cytokine Regulation in Human CD4 T Cells by the Aryl Hydrocarbon Receptor and Gq-Coupled Receptors. *Sci. Reports 2018 81*. **8**, 1–12 (2018).

48. V. Rothhammer, D. M. Borucki, E. C. Tjon, M. C. Takenaka, C.-C. Chao, A. Ardura-Fabregat, K. Alves de Lima, C. Gutiérrez-Vázquez, P. Hewson, O. Staszewski, M. Blain, L. Healy, T. Neziraj, M. Borio, M. Wheeler, L. Lionel Dragin, D. A. Laplaud, J. Antel, J. Ivan Alvarez, M. Prinz, F. J. Quintana, Microglial control of astrocytes in response to microbial metabolites (2018), doi:10.1038/s41586-018-0119-x.

49. V. Rothhammer, I. D. Mascanfroni, L. Bunse, M. C. Takenaka, J. E. Kenison, L. Mayo, C. C. Chao, B. Patel, R. Yan, M. Blain, J. I. Alvarez, H. Kébir, N. Anandasabapathy, G. Izquierdo, S. Jung, N. Obholzer, N. Pochet, C. B. Clish, M. Prinz, A. Prat, J. Antel, F. J. Quintana, Type i interferons and microbial metabolites of tryptophan modulate astrocyte activity and central nervous system inflammation via the aryl hydrocarbon receptor. *Nat. Med.* **22** (2016), doi:10.1038/nm.4106.

50. A. Parker, S. Fonseca, S. R. Carding, Gut microbes and metabolites as modulators of blood-brain barrier integrity and brain health. *Gut Microbes*. **11**, 135 (2020).

51. C. E. Keogh, D. H. J. Kim, M. M. Pusceddu, T. A. Knotts, G. Rabasa, J. A. Sladek, M. T. Hsieh, M. Honeycutt, I. Brust-Mascher, M. Barboza, M. G. Gareau, Myelin as a regulator of development of the microbiota-gut-brain axis. *Brain. Behav. Immun.* **91**, 437–450 (2021).

52. A. E. Hoban, R. M. Stilling, F. J. Ryan, F. Shanahan, T. G. Dinan, M. J. Claesson, G. Clarke, J. F. Cryan, Regulation of prefrontal cortex myelination by the microbiota. *Transl. Psychiatry*. **6** (2016), doi:10.1038/TP.2016.42.

53. N. Y. Lycke, M. Bemark, The regulation of gut mucosal IgA B-cell responses: recent developments. *Mucosal Immunol. 2017 106*. **10**, 1361–1374 (2017).

54. B. Vaidyanathan, A. Chaudhry, W. T. Yewdell, D. Angeletti, W. F. Yen, A. K. Wheatley, C. A. Bradfield, A. B. McDermott, J. W. Yewdell, A. Y. Rudensky, J. Chaudhuri, The aryl hydrocarbon receptor controls cell-fate decisions in B cells. *J. Exp. Med.* **214**, 197 (2017).

55. A. Araujo, A. Safronova, E. Burger, A. López-Yglesias, S. Giri, E. T. Camanzo, A. T. Martin, S. I. Grivennikov, F. Yarovinsky, Ifn-g mediates paneth cell death via suppression of mtor. *Elife*. **10** (2021), doi:10.7554/ELIFE.60478.

56. M. Kamioka, Y. Goto, K. Nakamura, Y. Yokoi, R. Sugimoto, S. Ohira, Y. Kurashima, S. Umemoto, S. Sato, J. Kunisawa, Y. Takahashi, S. E. Domino, J. C. Renauld, S. Nakae, Y. Iwakura, P. B. Ernst, T. Ayabe, H. Kiyono, Intestinal commensal microbiota and cytokines regulate Fut2+ Paneth cells for gut defense. *Proc. Natl. Acad. Sci. U. S. A.* **119** (2022), doi:10.1073/PNAS.2115230119/SUPPL_FILE/PNAS.2115230119.SAPP.PDF.

57. B. JG, T. MV, D. NL, O. S, S. JA, G. E, B. D, C. G, C. HS, H. X, W. L, C. AB, P. DA, R. NR, Č. D, Regulation of autoimmune myocarditis by host responses to the microbiome. *Exp. Mol. Pathol.* **103**, 141–152 (2017).

58. A. S. Bergot, R. Giri, R. Thomas, The microbiome and rheumatoid arthritis. *Best Pract. Res. Clin. Rheumatol.* (2020), doi:10.1016/J.BERH.2020.101497.

59. G. KL, A. BP, Q. EMM, The microbiome and inflammatory bowel disease. *J. Allergy Clin. Immunol.* **145**, 16–27 (2020).

60. O.-R. J, K. TO, K. LH, The Gut Microbiome and Multiple Sclerosis. *Cold Spring Harb. Perspect. Med.* **8** (2018), doi:10.1101/CSHPERSPECT.A029017.

61. H. YJ, B. HA, The microbiome in asthma. *J. Allergy Clin. Immunol.* **135**, 25–30 (2015).

62. T. Y. Chuang, Y. Guo, S. M. Seki, A. M. Rosen, D. M. Johanson, J. W. Mandell, C. F. Lucchinetti, A. Gaultier, LRP1 expression in microglia is protective during CNS autoimmunity. *Acta Neuropathol. Commun.* **4**, 68 (2016).

63. D. G. Remick, G. R. Bolgos, J. Siddiqui, J. Shin, J. A. Nemzek, Six at six: interleukin-6 measured 6 h after the initiation of sepsis predicts mortality over 3 days. *Shock*. **17**, 463–467 (2002).

64. S. M. Seki, M. Stevenson, A. M. Rosen, S. Arandjelovic, L. Gemta, T. N. J. Bullock, A. Gaultier, Lineage-Specific Metabolic Properties and Vulnerabilities of T Cells in the Demyelinating Central Nervous System. *J. Immunol.* **198**, 4607–4617 (2017).

65. P. Castellano-Escuder, C. Andrés-Lacueva, A. Sánchez-Pla, POMA: User-friendly Workflow for Metabolomics and Proteomics Data Analysis (2021), (available at https://github.com/pcastellanoescuder/POMA).

66. A. L. Hartman, D. M. Lough, D. K. Barupal, O. Fiehn, T. Fishbein, M. Zasloff, J. A. Eisen, Human gut microbiome adopts an alternative state following small bowel transplantation. *Proc. Natl. Acad. Sci. U. S. A.* **106**, 17187–17192 (2009).

67. D. K. Barupal, P. K. Haldiya, G. Wohlgemuth, T. Kind, S. L. Kothari, K. E. Pinkerton, O. Fiehn, MetaMapp: mapping and visualizing metabolomic data by integrating information from biochemical pathways and chemical and mass spectral similarity. *BMC Bioinformatics*. **13**, 1–15 (2012).

68. E. Bolyen, J. R. Rideout, M. R. Dillon, N. A. Bokulich, C. C. Abnet, G. A. Al-Ghalith, H. Alexander, E. J. Alm, M. Arumugam, F. Asnicar, Y. Bai, J. E. Bisanz, K. Bittinger, A. Brejnrod, C. J. Brislawn, C. T. Brown, B. J. Callahan, A. M. Caraballo-Rodríguez, J. Chase, E. K. Cope, R. Da Silva, C. Diener, P. C. Dorrestein, G. M. Douglas, D. M. Durall, C. Duvallet, C. F. Edwardson, M. Ernst, M. Estaki, J. Fouquier, J. M. Gauglitz, S. M. Gibbons, D. L. Gibson, A. Gonzalez, K. Gorlick, J. Guo, B. Hillmann, S. Holmes, H. Holste, C. Huttenhower, G. A. Huttley, S. Janssen, A. K. Jarmusch, L. Jiang, B. D. Kaehler, K. Bin Kang, C. R. Keefe, P. Keim, S. T. Kelley, D. Knights, I. Koester, T. Kosciolek, J. Kreps, M. G. I. Langille, J. Lee, R. Ley, Y. X. Liu, E. Loftfield, C. Lozupone, M. Maher, C. Marotz, B. D. Martin, D. McDonald, L. J. McIver, A. V. Melnik, J. L. Metcalf, S. C. Morgan, J. T. Morton, A. T. Naimey, J. A. Navas-Molina, L. F. Nothias, S. B. Orchanian, T. Pearson, S. L. Peoples, D. Petras, M. L. Preuss, E. Pruesse, L. B. Rasmussen, A. Rivers, M. S. Robeson, P. Rosenthal, N. Segata, M. Shaffer, A. Shiffer, R. Sinha, S. J. Song, J. R. Spear, A. D. Swafford, L. R. Thompson, P. J. Torres, P. Trinh, A. Tripathi, P. J. Turnbaugh, S. Ul-Hasan, J. J. J. van der Hooft, F. Vargas, Y. Vázquez-Baeza, E. Vogtmann, M. von Hippel, W. Walters, Y. Wan, M. Wang, J. Warren, K. C. Weber, C. H. D. Williamson, A. D. Willis, Z. Z. Xu, J. R. Zaneveld, Y. Zhang, Q. Zhu, R. Knight, J. G. Caporaso, Reproducible, interactive, scalable and extensible microbiome data science using QIIME 2. *Nat. Biotechnol. 2019 378*. **37**, 852–857 (2019).

69. B. J. Callahan, P. J. McMurdie, M. J. Rosen, A. W. Han, A. J. A. Johnson, S. P. Holmes, DADA2: High-resolution sample inference from Illumina amplicon data. *Nat. Methods 2016 137*. **13**, 581–583 (2016).

70. P. J. McMurdie, S. Holmes, phyloseq: An R Package for Reproducible Interactive Analysis and Graphics of Microbiome Census Data. *PLoS One*. **8**, e61217 (2013).

Acknowledgments: The authors wish to thank the University of Virginia Biorepository and Tissue Research facility for their support with immunohistochemistry.

The authors would also like to thank Tula Raghaven, Dr. Sanja Arandjelovic, and Dr. Sharon Walsh for critical reading and members the University of Virginia Brain Immunology and Glia Center for scientific input.

Funding:

National Institutes of Health grant R33 MH108156 (AG)

National Institutes of Health grant T32 NS115657 (ARM)

National Institutes of Health grant T32GM008136 (RMB)

The UVA Wagner fellowship (RMB)

The Owens Family Foundation (AG)

UVA Trans University Microbiome Initiative pilot grant (AG, ARM)

UVA Presidential Fellowship in Neuroscience (CRN)

Author contributions:

Conceptualization: ARM, AG

Methodology: ARM, AG

Data Collection: ARM, HJC, LCB, RMB, CRN, RMB

Data Analysis and Archiving: DGO

Supervision: AG

Writing—original draft: ARM, AG

Writing—review & editing: HJC, LCB, RMB, CRN, RMB, DGO

Competing interests:

Authors declare that they have no competing interests.

Data and materials availability:

All 16S sequencing data is publicly available on NCBI Gene Expression Omnibus accession number GSE200440. Metabolomics data and results of all statistical tests are available as supplement to the manuscript. All other raw data will be freely available upon request.

Figures:

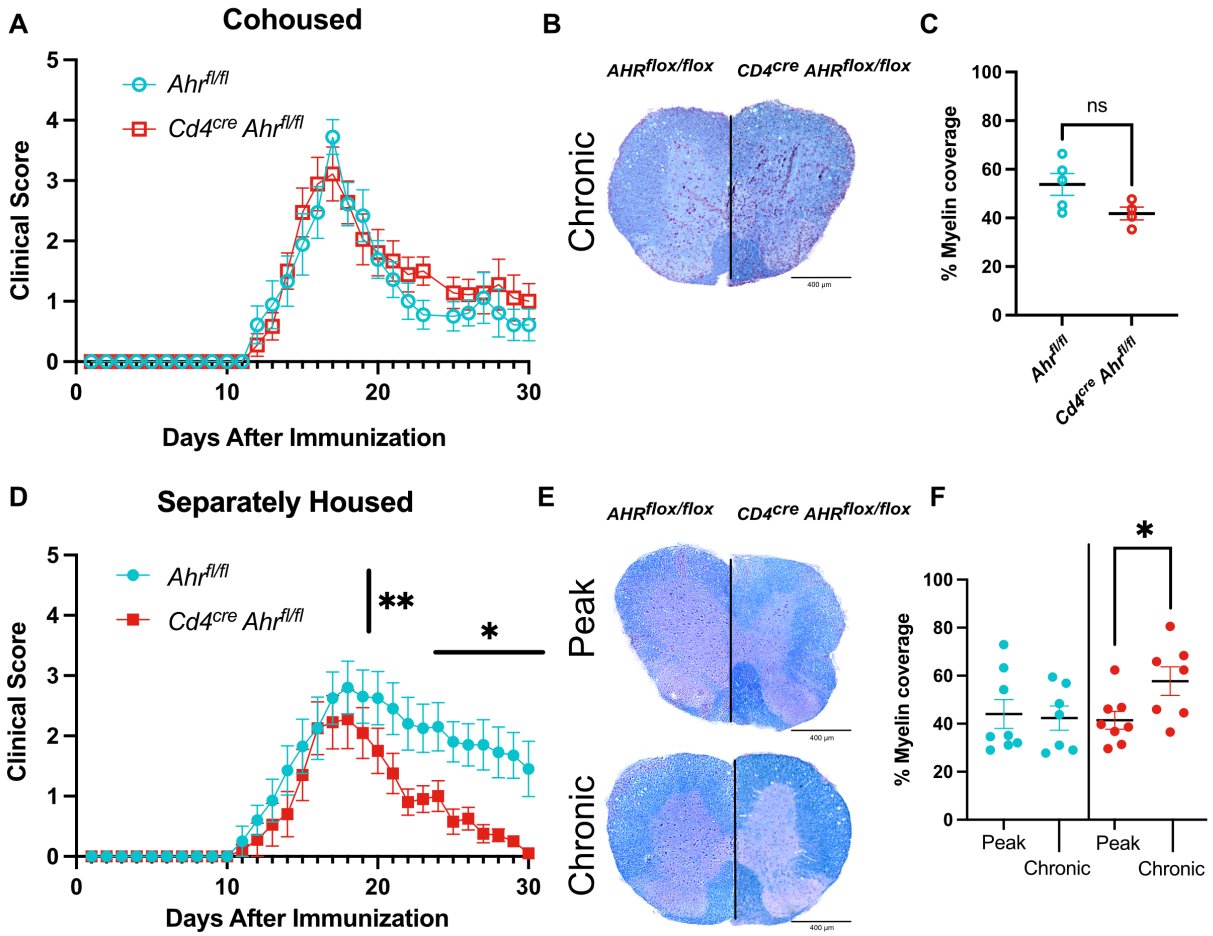

Fig. 1. **Separately housed *Cd4^cre^Ahr^fl/fl^* recover from EAE with increased myelin coverage at chronic phase.** (**A**) *Ahr* knockout in CD4+ cells does not change active EAE scores when animals are housed together. (Females; Representative plot includes n= 9/group; N=2) (**B**) Representative images of myelin coverage in the white matter of the spinal cord at Day 31 as measured by Luxol Fast Blue with Hematoxylin and Eosin stain. (**C**) Quantification of the white matter from images from four equally spaced spinal cord levels were averaged for each mouse. (n=5/group; Unpaired T test p=0.0706) (**D**) *Cd4^cre^Ahr^fl/fl^* separated from *Ahr^fl/fl^* littermate controls at weaning recover from EAE. (Females; Representative plot includes n=8-9/group; N=2; Mann-Whitney U Test on total

scores reported in legend [p=0.0096] and on single days reported on plot) (**E**) At the peak stage of EAE (Day 16), there are no differences in myelin coverage, but at chronic phase (Day 31) *Cd4*^{cre}*Ahr*$^{fl/fl}$ mice have more myelin coverage in the white matter than *Cd4*^{cre}*Ahr*$^{fl/fl}$ littermate controls. Representative images of myelin coverage in the white matter of the spinal cord as measured by Luxol Fast Blue with Hematoxylin and Eosin stain. (**F**) In support of clinical scores, quantification of myelin coverage shows that *Cd4*^{cre}*Ahr*$^{fl/fl}$ mice have myelin recovery by day 31 of EAE. (n=7-8 mice/group; N=2; Unpaired T tests [p=0.8343, 0.0322]) Scale bars represent 400µm. Error bars represent standard error from the mean.

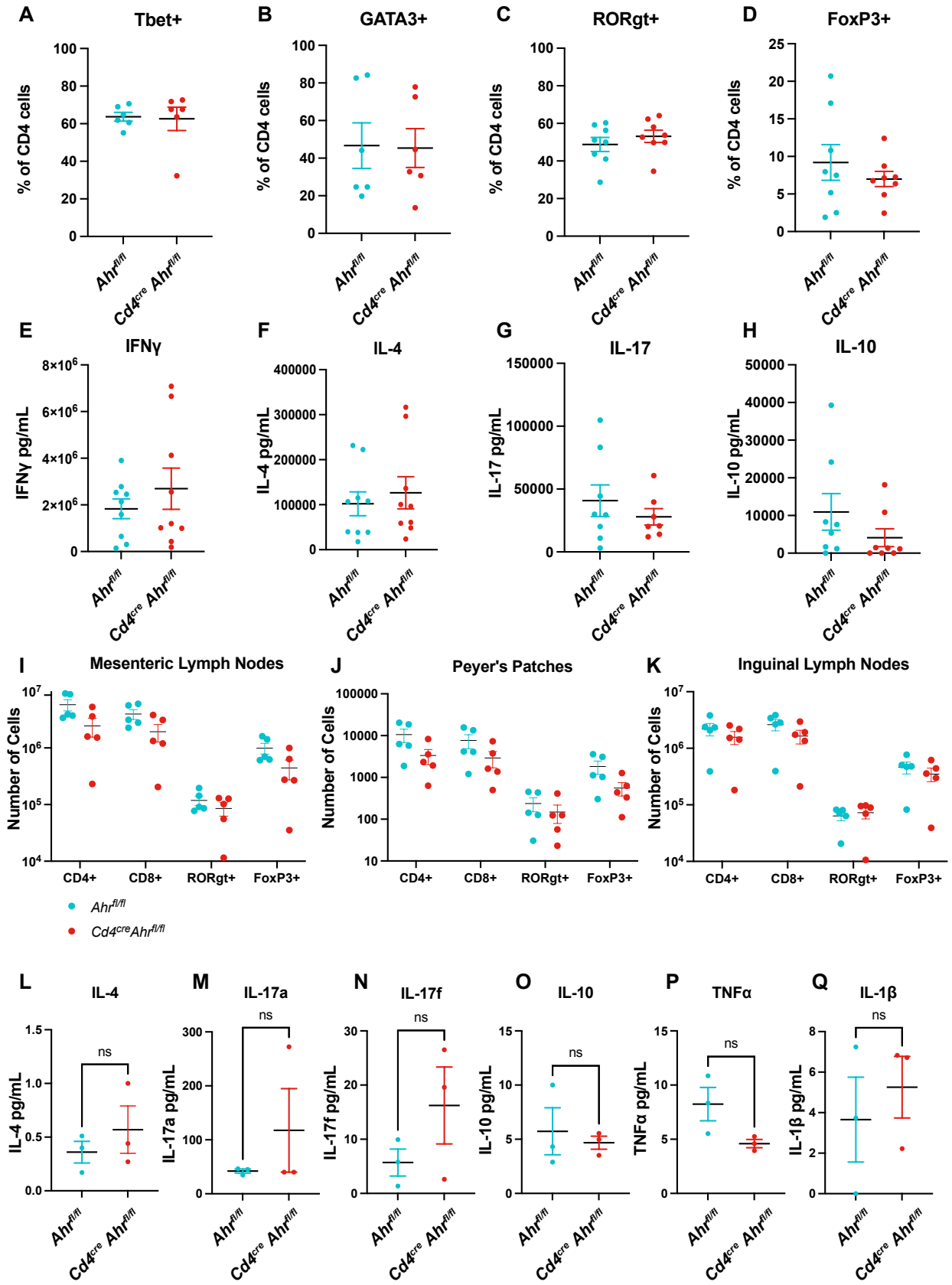
A
Tbet+
% of CD4 cells
B
GATA3+
% of CD4 cells
C
RORgt+
% of CD4 cells
D
FoxP3+
% of CD4 cells
E
IFNγ
IFNγ pg/mL
F
IL-4
IL-4 pg/mL
G
IL-17
IL-17 pg/mL
H
IL-10
IL-10 pg/mL
Ahr fl/fl
Cd4cre Ahr fl/fl
I
Mesenteric Lymph Nodes
J
Peyer's Patches
K
Inguinal Lymph Nodes
Number of Cells
CD4+
CD8+
RORgt+
FoxP3+
Ahr fl/fl
Cd4cre Ahr fl/fl
L
IL-4
IL-4 pg/mL
M
IL-17a
IL-17a pg/mL
N
IL-17f
IL-17f pg/mL
O
IL-10
IL-10 pg/mL
P
TNFα
TNFα pg/mL
Q
IL-1β
IL-1β pg/mL
ns

1

Fig. 2. *Ahr* knockout in CD4+ cells does not influence T cell differentiation (**A**) Naïve CD+ T cells were isolated from cohoused *Cd4*^{cre}*Ahr*$^{fl/fl}$ and littermate control animals and treated to promote differentiation to Th1 cell type. There is no difference in the percentage of Tbet+ Th1 cells measured by flow cytometry at the end of the skewing period. (n=6/group; N=2; Unpaired T test [p=0.8715]) This remains true for cells skewed toward (**B**) Th2 cells (n=6/group; N=2; Unpaired T test [p=0.9356]), (**C**) T_H17 cells (n=8/group; N=3; Unpaired T test [p=0.3989]) (**D**), and Treg cells (n=8/group; N=3; Unpaired T test [p=0.4078]). (**E**) ELISA analysis of culture supernatant after 24 hours of anti-CD3 stimulation in Th1 cells (n=8/group; N=3; Unpaired T test [p=0.3924]) (**F**) Th2 cells(n=8/group; N=3; Unpaired T test [p=0.5917]) (**G**) T_H17 cells (n=7-8/group; N=3; Unpaired T test [p=0.4013]) (**H**) or Treg cells. (n=8/group; N=3; Unpaired T test [p=0.2278]) (**I**) Flow cytometry of single cell suspensions of cohoused *Cd4*^{cre}*Ahr*$^{fl/fl}$ and *Ahr*$^{fl/fl}$ mice show no differences in the T cell composition of the mesenteric lymph nodes, (Multiple T tests with Welch correction [p=0.070748, 0.081520, 0.325104, 0.080798]) (**J**) the Peyer's patches, (Multiple T tests with Welch correction [p=0.127038, 0.179526, 0.444670, 0.118472]) (**K**) or the inguinal lymph nodes (Multiple T tests with Welch correction [p=0.381964, 0.224164, 0.664161, 0.465348]) (**L-Q**) Luminex assay on whole spinal cord homogenate of separately house *Cd4*^{cre}*Ahr*$^{fl/fl}$ and *Ahr*$^{fl/fl}$ mice at the peak of disease (Day 16 after immunization; n=3/group; N=1; Unpaired T test) (L) [p=0.7789] (M) [p=0.3851] (N) [p=0.2341] (O) [p=0.6635] (P) [p=0.0834] (Q) [p=0.5693] Error bars represent standard error from the mean.

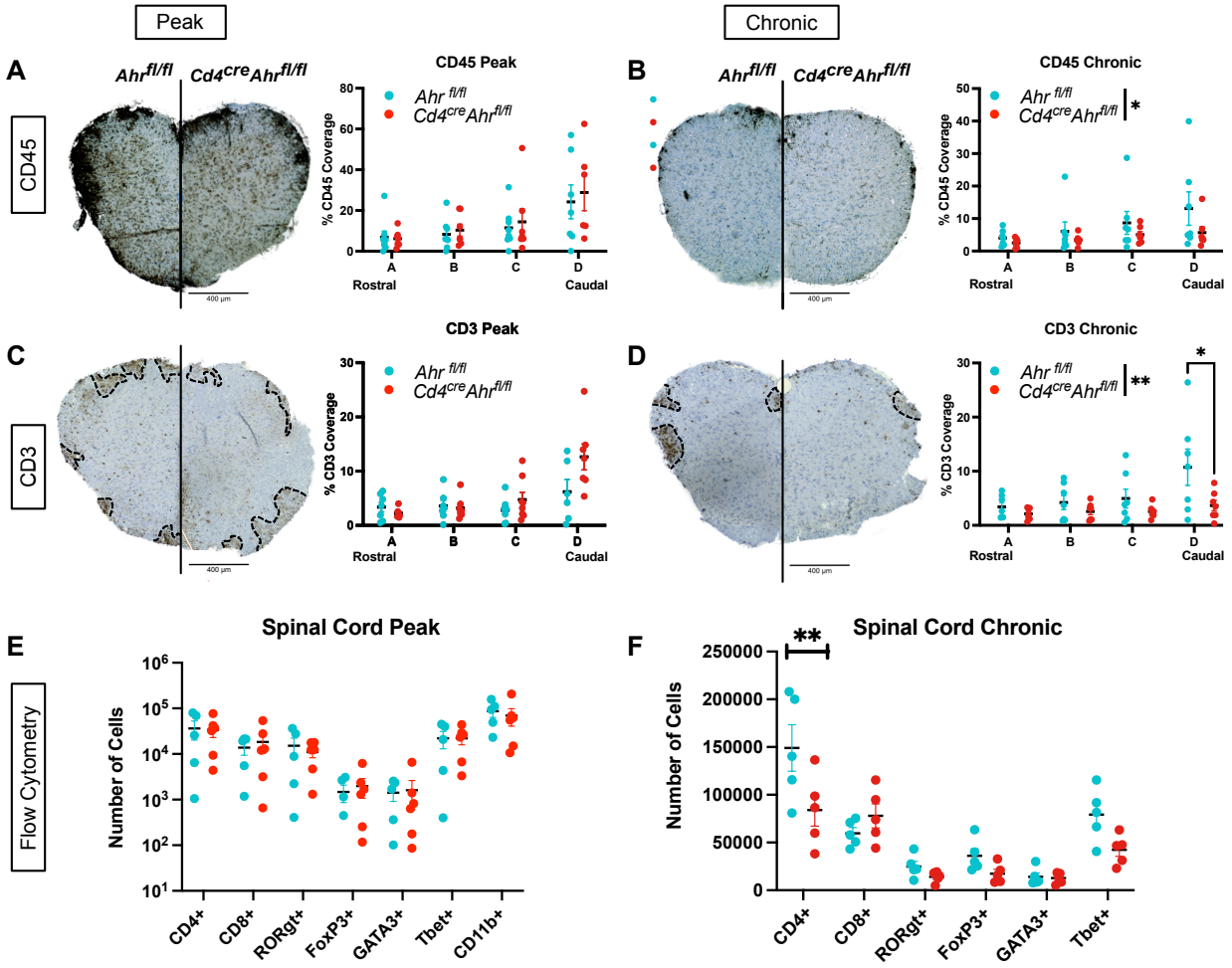

Fig. 3. Reduced CD3+ cells in the spinal cord of *Cd4^{cre}Ahr$^{fl/fl}$* mice at chronic phase. (**A**) No difference in CD45+ staining by immunohistochemistry at the peak of disease. Both *Cd4^{cre}Ahr$^{fl/fl}$* mice and *Ahr$^{fl/fl}$* littermate controls have equal number of CD45+ cells at Day 16 of EAE when separately housed. (Each dot represents a mouse n=7/group; N=2; Two-way ANOVA[p=0.5336]) (**B**) CD45 coverage was reduced in *Cd4^{cre}Ahr$^{fl/fl}$* mice and *Ahr$^{fl/fl}$* littermate controls at Day 31 (Two-way ANOVA [p=0.0419]; Sidak's multiple comparisons test [p=0.9896, 0.9209, 0.7898, 0.1753]) (**C**) Reflective of the clinical scores at peak of disease there is no difference in the presence of CD3+ cells (Two-way ANOVA [p=0.0830]), however, (**D**) by Day 31 there is significantly less CD3+ coverage in *Cd4^{cre}Ahr$^{fl/fl}$*

spinal cords at all levels compared to separately housed control mice. (n=7/group; N=2, Two-way ANOVA [p=0.0054]; Sidak's multiple comparisons test [p=0.9578, 0.9029, 0.7095, 0.0070]) (**E**) Flow cytometry analysis of isolated immune cells at Day 16 shows no difference in the number of T cells or macrophages present between genotypes. (n=5-6/group; Multiple Unpaired T Tests with Benjamini and Yekutieli corrections [p values listed in supplement]). (**F**) Day 31 spinal cord flow cytometry shows a specific reduction in CD4+ T cells in *Cd4*^{cre}*Ahr*$^{fl/fl}$ mice compared to separately housed *Ahr*$^{fl/fl}$ mice. There is no significant decrease in any single subpopulation of CD4+ T cells indicating that this loss is likely spread across subtypes. (n=5/group; Multiple Unpaired T Tests with Benjamini and Yekutieli corrections[p values listed in supplement]). Scale bars represent 400µm. Error bars represent standard error from the mean.

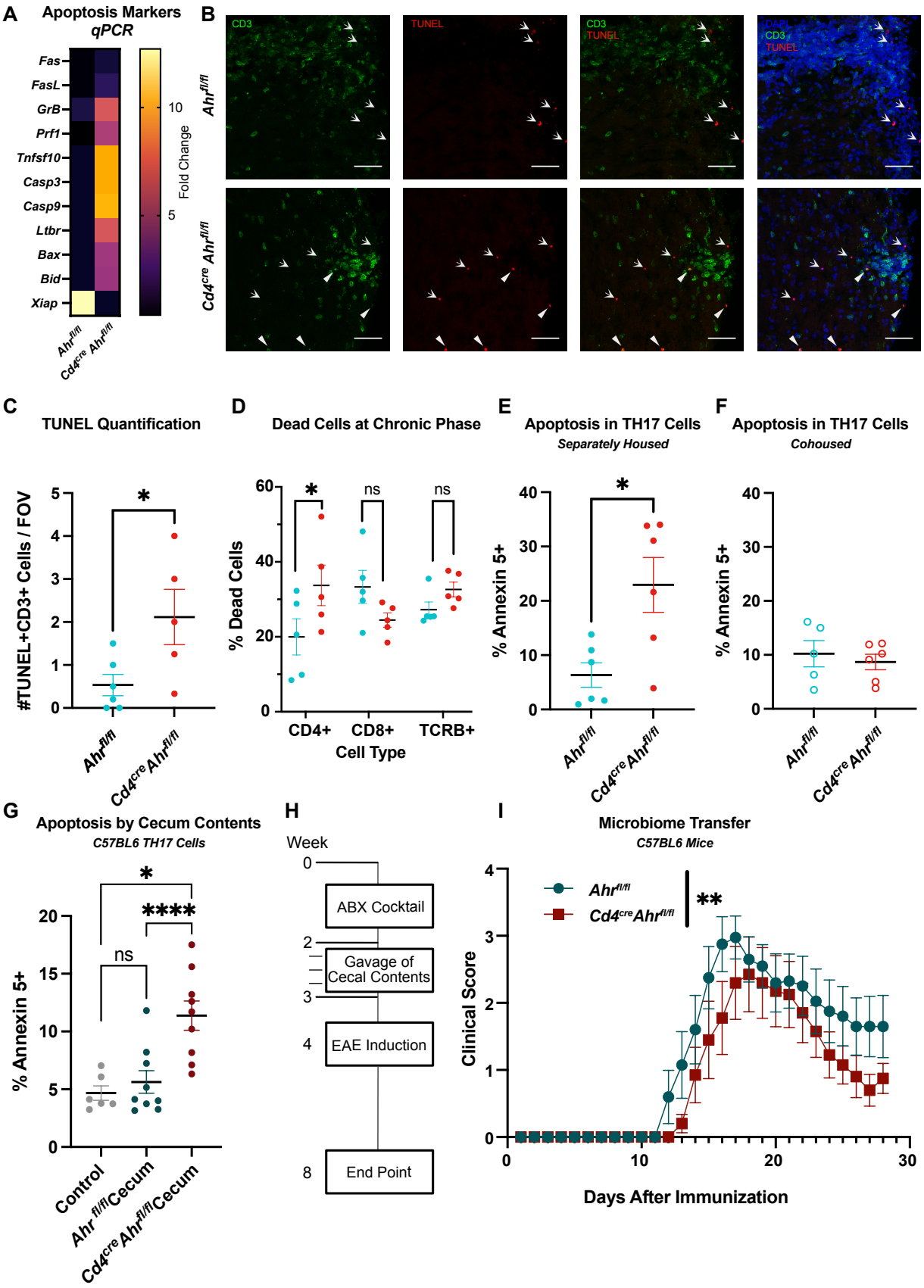
A
Apoptosis Markers
qPCR
Fas
FasL
GrB
Prf1
Tnfsf10
Casp3
Casp9
Ltbr
Bax
Bid
Xiap
Fold Change
10
5
Ahr fl/fl
Cd4cre Ahr fl/fl
B
CD3
TUNEL
DAPI
C
TUNEL Quantification
#TUNEL+CD3+ Cells / FOV
D
Dead Cells at Chronic Phase
% Dead Cells
CD4+
CD8+
TCRB+
Cell Type
ns
E
Apoptosis in TH17 Cells
Separately Housed
% Annexin 5+
F
Apoptosis in TH17 Cells
Cohoused
G
Apoptosis by Cecum Contents
C57BL6 TH17 Cells
Control
Ahr fl/fl Cecum
Cd4cre Ahr fl/fl Cecum
H
Week
ABX Cocktail
Gavage of Cecal Contents
EAE Induction
End Point
I
Microbiome Transfer
C57BL6 Mice
Clinical Score
Days After Immunization

1

Fig 4. T cell apoptosis increased in animals who recover from EAE (**A**) Gene expression analysis (qPCR array) performed on spinal cord RNAs prepared from separately housed *Cd4*^{cre}*Ahr*$^{fl/fl}$ mice and *Ahr*$^{fl/fl}$ littermate controls at the peak of disease (Day 16) shows increased pro-apoptotic transcripts and decreased anti-apoptotic transcript. (**B**) Representative image of spinal cords stained with TUNEL and T cell marker at the peak of disease (CD3). Closed triangles indicate TUNEL+CD3+ cells and arrowheads indicate TUNEL+CD3- cells. Scale bar = 400µm. (**C**) Quantification of the number of TUNEL+ T cells (2-6 lesion sites averaged per animal; n=5-6 animals; N=2; Unpaired T test [p=0.0357])**(D)** T cells isolated from the spinal cord at the peak of disease stained with viability dye and measured by flow cytometry reveal differences in death are limited to the CD4+ compartment **(**n=5/group; Two-way ANOVA [p=0.0192] with Sidak's Multiple Comparison Tests [p=0.0465, 0.2862, 0.6800]) (**E**) T cells skewed to T_H17 *in vitro* from separately housed *Cd4*^{cre}*Ahr*$^{fl/fl}$ mice have higher levels of the apoptotic marker Annexin 5 after 24 hours of CD3 stimulation. (n=6/group; N=2; Unpaired T test [p=0.0133]) (**F**) T_H17 cells from cohoused *Cd4*^{cre}*Ahr*$^{fl/fl}$ and *Ahr*$^{fl/fl}$ mice show no differences in apoptosis after stimulation. (n=5-6/group; N=2; Unpaired T test [p=0.5851]).(**G**) Skewed T_H17 cells from C57BL6/J mice that are exposed to the <3kDa fraction of cecal contents from only *Cd4*^{cre}*Ahr*$^{fl/fl}$ mice have high levels of apoptosis. (n=6-9/group; N=3; Mixed-effects analysis, with Geisser-Greenhouse correction [p=0.0013]; Tukey's post hoc analysis [Ctr v Fl p=0.7729; Ctr v Cre p=0.0333, Fl v Cre p<0.0001]) (**H**) Protocol for microbiome transfer from separately housed *Cd4*^{cre}*Ahr*$^{fl/fl}$ and *Ahr*$^{fl/fl}$ mice to C57BL6/J mice. (**I**)

Microbiome transfer from *Cd4*^{cre}*Ahr*$^{fl/fl}$ mice sufficient to drive the recovery from EAE in wildtype mice (Females; Representative plot includes n= 10/group; N=2; Mann-Whitney U Test on total scores [p=0.0126]). Error bars represent standard error from the mean.

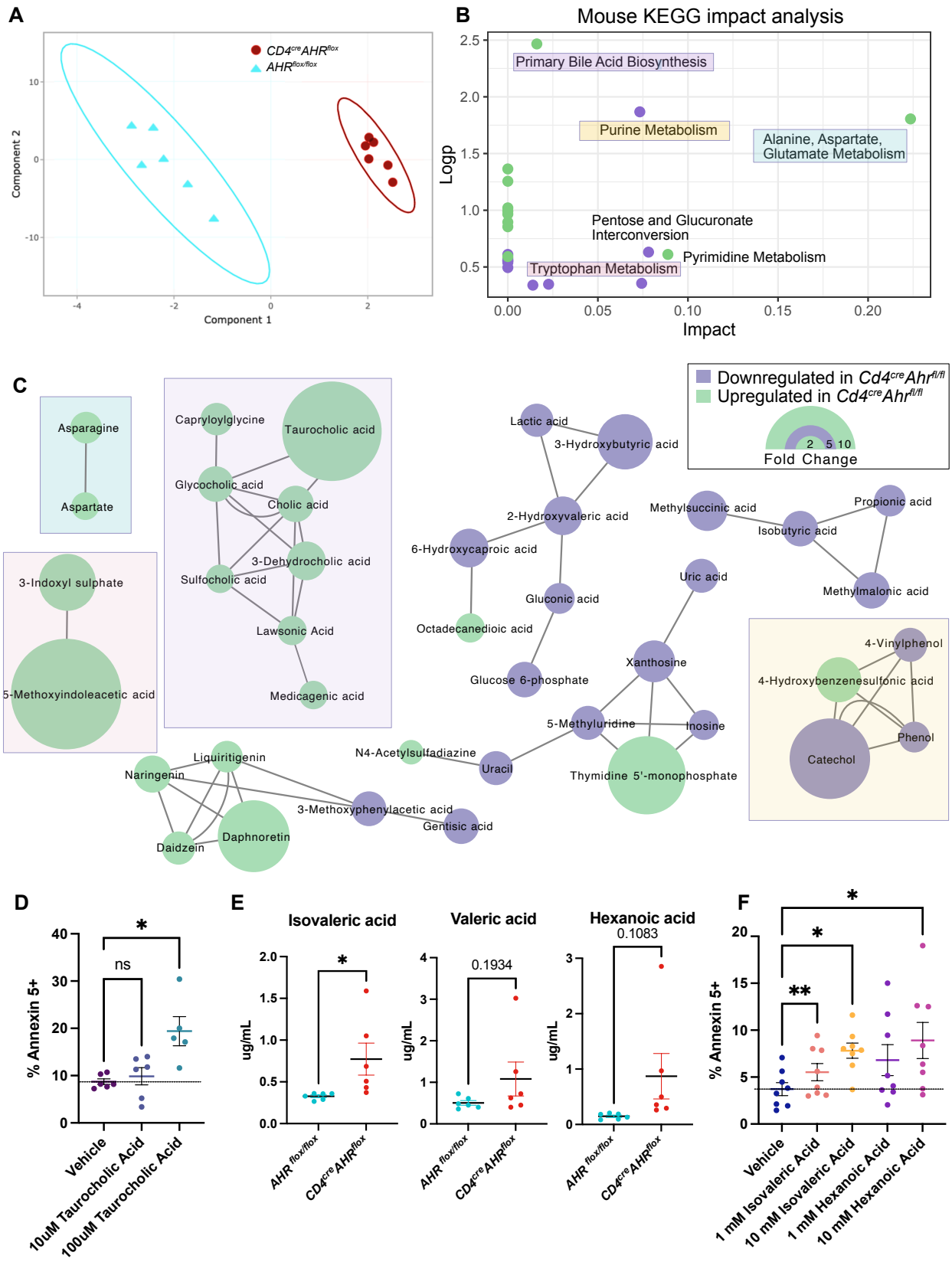
A
CD4cre AHRflox
AHRflox/flox
Component 2
Component 1
B
Mouse KEGG impact analysis
Primary Bile Acid Biosynthesis
Purine Metabolism
Alanine, Aspartate, Glutamate Metabolism
Pentose and Glucuronate Interconversion
Pyrimidine Metabolism
Tryptophan Metabolism
Logp
Impact
C
Downregulated in Cd4cre Ahrfl/fl
Upregulated in Cd4cre Ahrfl/fl
Fold Change
Asparagine
Aspartate
3-Indoxyl sulphate
5-Methoxyindoleacetic acid
Capryloylglycine
Taurocholic acid
Glycocholic acid
Cholic acid
3-Dehydrocholic acid
Sulfocholic acid
Lawsonic Acid
Medicagenic acid
Lactic acid
3-Hydroxybutyric acid
2-Hydroxyvaleric acid
6-Hydroxycaproic acid
Gluconic acid
Octadecanedioic acid
Glucose 6-phosphate
Methylsuccinic acid
Propionic acid
Isobutyric acid
Methylmalonic acid
Uric acid
Xanthosine
5-Methyluridine
Inosine
Thymidine 5'-monophosphate
Uracil
N4-Acetylsulfadiazine
4-Vinylphenol
4-Hydroxybenzenesulfonic acid
Phenol
Catechol
Liquiritigenin
Naringenin
Daidzein
Daphnoretin
3-Methoxyphenylacetic acid
Gentisic acid
D
% Annexin 5+
ns
Vehicle
10uM Taurocholic Acid
100uM Taurocholic Acid
E
Isovaleric acid
Valeric acid
Hexanoic acid
0.1934
0.1083
ug/mL
AHR flox/flox
CD4cre AHRflox
F
% Annexin 5+
Vehicle
1 mM Isovaleric Acid
10 mM Isovaleric Acid
1 mM Hexanoic Acid
10 mM Hexanoic Acid

1

Fig 5. Elevated bile salts and SCFA detected in the cecum of AHR deficient mice drive T cell apoptosis(**A**) Partial least-squares plot of LC-MS untargeted metabolomics of the <3kDa fraction of the cecal contents from *Cd4*^{cre}*Ahr*$^{fl/fl}$ and *Ahr*$^{fl/fl}$ mice. (**B**) Metaboanalyst mouse KEGG pathways significantly changed by genotype. (**C**) MetaMapp network analysis visualizing the chemically or biologically related significantly change molecules. (**D**) Taurocholic acid (100μM) is sufficient to drive apoptosis in T_H17 cells isolated from C57BL6/J mice. (n=5-6; N=2; Mixed effects analysis with Geisser-Greenhouse correction [p=0.0070]; Dunnett's multiple comparison test [Veh vs 10μM p=0.8178, Veh vs 100μM p=0.0233]) (**E**) Quantitative targeted metabolomics for short chain fatty acids show a significant increase in isovaleric acid, and a trending increase in valeric and hexanoic acid in *Cd4*^{cre}*Ahr*$^{fl/fl}$ mice. (n=6; N=1; Unpaired T tests [p=0.0427, 0.1934, 0.1083]) (**F**) Administration of isovaleric acid and Hexanoic acid are sufficient to drive apoptosis in T_H17 cells isolated from C57BL6/J mice. (n=8; N=2; RM one-way ANOVA with the Geisser-Greenhouse correction[p=0.0399] Dunnett's multiple comparisons test [Veh vs 1mM Hexanoic p=0.0764, Veh vs 10mM Hexanoic p=0.0352, Veh vs 1mM Isovaleric p=0.0026, Veh vs 10mM Isovaleric p=0.0254]). Error bars represent standard error from the mean.